The Astrophysical Journal, 949:93 (14pp), 2023 June 1 https://doi.org/10.3847/1538-4357/acc5e7

Inferring the Progenitor Mass–Kinetic Energy Relation of Stripped-envelope Core-collapse Supernovae from Nebular Spectroscopy

Qiliang Fang (方其亮) and Keiichi Maeda
Department of Astronomy, Kyoto University, Kitashirakawa-Oiwake-cho, Sakyo-ku, Kyoto 606-8502, Japan; fangql@kusastro.kyoto-u.ac.jp
Received 2022 December 15; revised 2023 March 17; accepted 2023 March 17; published 2023 June 1

Abstract

The relation between the progenitor mass and the kinetic energy of the explosion is a key toward revealing the explosion mechanism of stripped-envelope core-collapse supernovae (SESNe). Here, we present a method to derive this relation using the nebular spectra of SESNe, based on the correlation between [O I]/[Ca II], which is an indicator of progenitor mass, and the width of [O I], which measures the expansion velocity of the oxygen-rich material. To explain the correlation, the kinetic energy ($E_{\rm K}$) is required to be positively correlated with the progenitor mass as represented by the CO core mass ($M_{\rm CO}$). We demonstrate that SNe IIb/Ib and SNe Ic/Ic-BL follow the same $M_{\rm CO}$–$E_{\rm K}$ scaling relation, which suggests that helium-rich and helium-deficient SNe share the same explosion mechanism. The $M_{\rm CO}$–$E_{\rm K}$ relation derived in this work is compared with the ones derived from early phase observations. The results are largely in good agreement. Combined with early phase observations, the method presented in this work provides a chance to scan through the ejecta from the outermost region to the dense inner core, which is important to reveal the global properties of the ejecta and constrain the explosion mechanism of core-collapse SNe.

Unified Astronomy Thesaurus concepts: Core-collapse supernovae (304); Type Ib supernovae (1729); Type Ic supernovae (1730); Supernova dynamics (1664)

1. Introduction

Core-collapse supernovae (CCSNe) mark the final stage of the evolution of a massive star with a zero-age main-sequence (ZAMS) mass larger than 8 $M_{\odot}$. The explosion mechanism of this catastrophic event has yet to be clarified. How the properties of the explosion process depends on those of the progenitor is an important open problem in astronomy.

CCSNe have diverse observable signatures, leading to classification into different subtypes. Type II supernovae (SNe II) show strong hydrogen features in their optical spectra. CCSNe lacking permanent hydrogen signatures are classified as stripped-envelope supernovae (SESNe). Among them, type Ib SNe (SNe Ib) do not exhibit hydrogen features, but their spectra are dominated by helium features. The spectra of type Ic SNe (SNe Ic) lack both hydrogen and helium features. Type IIb SNe (SNe IIb) are transitional events between SNe II and Ib; SNe IIb initially show strong hydrogen signatures, but their spectra eventually resemble to those of SNe Ib as the ejecta continue to evolve. SNe Ic can be further classified as normal SNe Ic and broad-line SNe Ic (SNe Ic-BL). The latter type is characterized by broad absorption features and its (occasional) association with a gamma-ray burst (Galama et al. 1998; Nakamura et al. 2001; Mazzali et al. 2002; Hjorth et al. 2003; Woosley & Bloom 2006). The readers are referred to Filippenko (1997), Gal-Yam (2017), and Modjaz et al. (2019) for the classification of SNe. The lack of hydrogen (or helium) in the spectra of SESNe indicates that the hydrogen-rich envelope (or the helium-rich layer) has been stripped away before the explosion. Several channels may be responsible for preSN mass loss, including binary interaction, stellar wind, or a combination of both (Heger et al. 2003; Sana et al. 2012; Groh et al. 2013; Smith 2014; Yoon 2015; Fang et al. 2019).

Understanding how the explosion process is dependent on the state of the progenitor is a key toward revealing the explosion mechanism of CCSNe. We thus need independent measurements of the progenitor properties and the explosion parameters. The relation between the two basic parameters, i.e., the progenitor mass and the amount of the kinetic energy, is particularly important but not established. The main difficulty comes from mapping the observables to these two quantities. Obtaining preexplosion images, which allow one to identify directly the progenitor (therefore providing a robust measurement of the mass), is only feasible for a very limited sample of CCSNe, and especially lacking for SESNe (Maund et al. 2011; Cao et al. 2013; Van Dyk et al. 2014; see also Smartt 2009 for a review). So far preexplosion images have only been available for two SNe Ib (iPTF 13bvn, Bersten et al. 2014; SN 2019yvr, Kilpatrick et al. 2021). Currently, modeling of the bolometric light curve is the main tool to infer the properties of the progenitor and the explosion, and most of them are based on the model established by Arnett (1982). For hydrogen-poor SNe, the ejecta are mainly powered by the decay of radioactive ^{56}Ni/Co, and the diffusion timescale of the photons generated by the decay chain determines the width of the light curve. With the photospheric velocity compiled from spectra at maximum light, the ejecta mass, the kinetic energy, and their mutual relation can be determined. However, previous research based on this method was mainly conducted at the photospheric phase, i.e., the period during which the ejecta are still optically thick, and the analyses constrain the nature of the outermost region of the ejecta. The interpretation regarding the global properties of the ejecta thus relies on extrapolation of the ejecta properties inward.

In this work, we propose a complementary method to constrain the relation between the progenitor mass and the kinetic energy of SESNe, based on observations at the nebular phase, i.e., several months after the explosion when the ejecta becomes transparent. Fang et al. (2022) reported a correlation between the [O I]/[Ca II] ratio, which serves as an indicator of progenitor mass (Fransson & Chevalier 1989; Jerkstrand et al. 2015; Kuncarayakti et al. 2015; Jerkstrand 2017; Fang & Maeda 2018; Fang et al. 2019; Dessart et al. 2021; Fang et al. 2022), and the [O I] width, which measures the characteristic expansion velocity of the oxygen-rich material (Taubenberger et al. 2009; Maurer et al. 2010; Fang et al. 2022), using a large sample of nebular spectra of 103 SESNe. In contrast to observations at the photospheric phase, nebular phase observations are sensitive to the properties in the dense innermost region where the explosion is initialized, and thus the explosion mechanism.

To build up the connection between the progenitor CO core mass ($M_{\rm CO}$) and the kinetic energy ($E_{\rm K}$) from a theoretical aspect, we explode a helium star and CO star models generated by the one-dimensional stellar evolution code, Modules for Experiments in Stellar Astrophysics (MESA; Paxton et al. 2011, 2013, 2015, 2018, 2019), with a wide range of kinetic energy injected, using the SuperNova Explosion Code (SNEC; Morozova et al. 2015). Omitting detailed spectrum synthesis calculations which would require massive computations, including a detailed treatment of the nonlocal thermal equilibrium (non-LTE), we focus on the scaling relations between the model and the observed quantities. We especially apply the relation between the [O I]/[Ca II] ratio and the oxygen mass $M_{\rm O}$ based on the specific models by Jerkstrand et al. (2015). The properly weighted velocity is linked to the observed line width. The $M_{\rm CO}$–$E_{\rm K}$ relation is then established by linking the models to the [O I]/[Ca II]–[O I] width correlation.

Finally, the $M_{\rm CO}$–$E_{\rm K}$ relation established from nebular phase observations is compared to those derived from early phase observations. The early phase and late phase observations are indeed probing different regions of the ejecta. The combined analysis of the observations from these two periods thus provides us with a unique chance to scan through the ejecta from the outermost layer to the innermost region, which will be useful to reconstruct the full ejecta structure. Further, any possible inconsistency between the analyses based on the early phase and nebular phase observations will help to clarify what is still missing in the current assumptions of the ejecta structure, and improve our understanding of the ejecta dynamics.

The paper is organized as follows. In Section 2, we describe the numerical approaches, including the generation of the progenitor models, the mixing scheme, and the setup of the explosion. In Section 3, we introduce how the model quantities are connected to the observables, and derive the quantitative $M_{\rm CO}$–$E_{\rm K}$ relation based on the [O I]/[Ca II]–[O I] width correlation. The possible affecting factors, including the dependence of [O I]/[Ca II] on $E_{\rm K}$ and the degree of microscopic mixing, and the effect of macroscopic mixing on the line width, are discussed in Section 4. The $M_{\rm CO}$–$E_{\rm K}$ relation established in this work is compared with the ones derived from the early phase observation in Section 5. The paper is closed with a summary of our findings in Section 6.

2. Numerical Approaches

2.1. MESA: From Premain Sequence to CC

The SN progenitor models are calculated using the one-dimensional stellar evolution code MESA (Paxton et al. 2011, 2013, 2015, 2018, 2019). We start with MESA version 11701 test suites, and closely follow the setup of example_make_pre_ccsn with minor modification. The inlists in this test suite include all processes involved in massive star evolution, including pre–main-sequence evolution, gradual burning of elements, removal of the outermost layers and the hydrodynamics of the iron-core infall. The ZAMS masses ($M_{\rm ZAMS}$) are 13, 15, 18, 20, 23, 25, and 28 $M_\odot$. For all models, we fix the metallicity ($Z = 0.02$, i.e., solar metallicity) and mixing length ($\alpha_{\rm env} = 3.0$ in the hydrogen-rich envelope and 1.5 in the other regions). No rotation is introduced.

This paper mainly focuses on the preSN structure of a helium star (the progenitor of SNe IIb/Ib, if the hydrogen skin of SNe IIb is neglected) and a bare CO core (the progenitor of SNe Ic/Ic-BL); therefore the hydrogen envelope or the helium-rich layer should be removed before the explosion. There are several channels that may be responsible for the envelope-stripping process, i.e., binary mass transfer, stellar winds, or a combination of both (Heger et al. 2003; Sana et al. 2012; Groh et al. 2013; Smith 2014; Yoon 2015; Fang et al. 2019). However, after the helium burning is finished, the core structure will not be significantly affected by the presence or the absence of the outermost layers; therefore the detailed mass-loss mechanism is not important for the purpose of this work. The hydrogen envelope or the helium-rich layer is thus removed manually. We first evolve the star to the helium ignition phase without mass loss. After the helium in the center is exhausted, the mass-loss rate is manually changed to $10^{-3}\ M_\odot\ {\rm yr}^{-1}$ (or $10^{-4}\ M_\odot\ {\rm yr}^{-1}$) for the removal of the hydrogen envelope (or the helium-rich layer), until the hydrogen (or helium) mass drops below 0.01 $M_\odot$ (or 0.12 $M_\odot$). Observationally, it has been indicated that SNe Ic/Ic-BL have a larger progenitor CO core mass than SNe IIb/Ib (Fang et al. 2019, 2022; Sun et al. 2023); therefore the helium-rich layer is stripped only for models with $M_{\rm ZAMS}$ not less than 18 $M_\odot$. After the outer layers are removed, we calculate the subsequent evolution without mass loss until Fe CC. The inlists used to generate the progenitor models in this work are available on Zenodo under an open-source Creative Commons Attribution 4.0 International license: doi:10.5281/zenodo.7740506.

In the upper panel of Figure 1, we show the preSN density structures of helium stars with $M_{\rm ZAMS} = 13$, 18, and 23 $M_\odot$, and bare CO cores with $M_{\rm ZAMS} = 18$ and 23 $M_\odot$. The mass fractions of ^{4}He, ^{12}C, ^{16}O, and ^{24}Mg for the helium star with $M_{\rm ZAMS} = 20\ M_\odot$ are also plotted in the lower panel of Figure 1 for illustration.

Some properties of the progenitor models are summarized in Table 1. In this work, the outer boundary of the CO core is defined to be the mass coordinate with the helium mass fraction $X_{\rm He} = 0.5$ (as marked by the black star in the lower panel of Figure 1); the CO core mass ($M_{\rm CO}$) refers to the mass coordinate at the CO core outer boundary. The mass of the

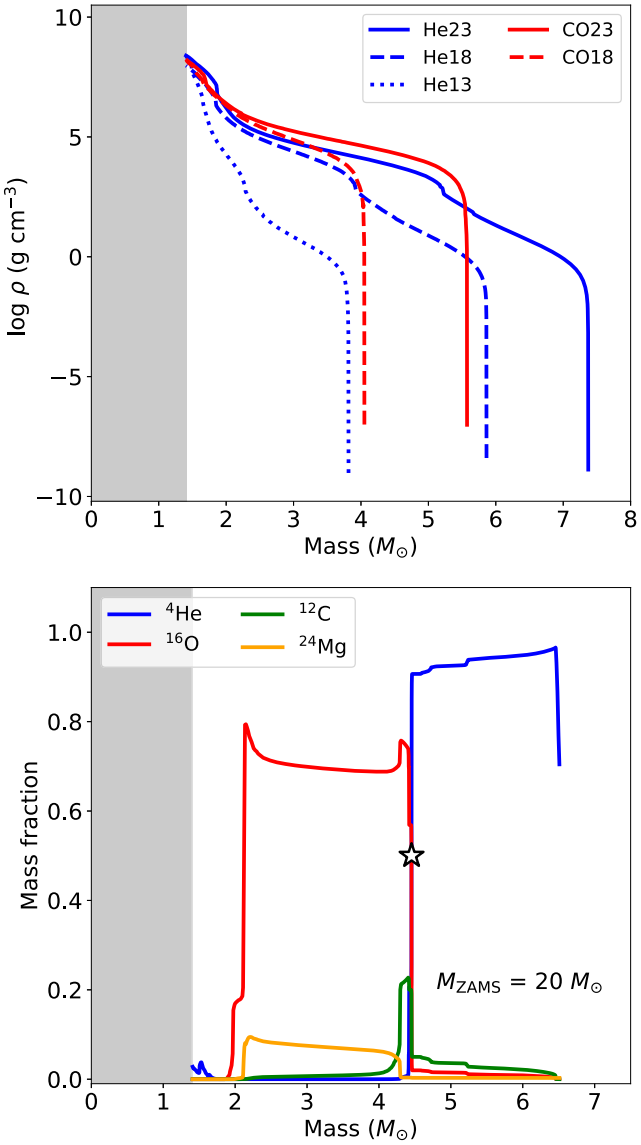

Figure 1. Upper panel: the density structures of He stars with $M_{\rm ZAMS} = 13$, 18, and 23 $M_\odot$ and the bare CO stars with $M_{\rm ZAMS} = 18$ and 23 $M_\odot$. Lower panel: the mass fractions of ^{4}He, ^{12}C, ^{16}O, and ^{24}Mg for the helium star with $M_{\rm ZAMS} = 20\,M_\odot$. The star marks the mass coordinate of the CO core boundary. The shaded regions in the two panels represent the region collapsing into the compact remnant.

oxygen is

$$M_{\rm O} = \sum X_{\rm O}(m_{\rm i})\Delta m_{\rm i}, \quad (1)$$

where $X_{\rm O}(m_{\rm i})$ is the oxygen mass fraction of the grid centered at $m_{\rm i}$. The CO core mass ($M_{\rm CO}$) is strongly correlated with $M_{\rm ZAMS}$. The linear regression (in logarithm scale) gives

$$M_{\rm CO} \propto M_{\rm ZAMS}^{1.53\pm0.05}. \quad (2)$$

The oxygen mass $M_{\rm O}$ is also correlated with $M_{\rm CO}$, and scales as

$$M_{\rm O} \propto M_{\rm CO}^{1.74\pm0.10}. \quad (3)$$

The above correlations are plotted in Figure 2. The effect of the attached helium-rich layer on the CO core properties is negligible.

Table 1
Summary of the PreSN Model Properties in this Study

Model	$M_{\rm ZAMS}$	$M_{\rm pre-SN}$	$M_{\rm CO}$	$M_{\rm env}$	$M_{\rm O}$
He13	13	3.82	2.27	1.55	0.43
He15	15	4.74	2.99	1.75	0.89
He18	18	5.86	3.90	1.96	1.50
He20	20	6.51	4.45	2.06	1.70
He23	23	7.37	5.18	2.20	2.56
He25	25	8.88	6.57	2.31	3.37
He28	28	9.96	7.45	2.51	3.47
CO18	18	4.05	3.94	⋯	1.29
CO20	20	4.67	4.58	⋯	1.96
CO23	23	5.57	5.49	⋯	2.48
CO25	25	6.74	6.62	⋯	3.13
CO28	28	7.67	7.54	⋯	3.92

Note. The helium star models (prefix "He") are listed at the upper part and the CO star models (prefix "CO") are at the lower part. For each model, we give the ZAMS mass ($M_{\rm ZAMS}$), the mass at CC ($M_{\rm pre-SN}$), the CO core mass defined by $X_{\rm He} = 0.5$ ($M_{\rm CO}$), the mass of the helium-rich layer ($M_{\rm env}$), and the total oxygen mass in the ejecta ($M_{\rm O}$). These quantities are all in the unit of solar mass $M_\odot$.

In the following, we use the term HeXX (or COXX) to represent a helium star (or bare CO star) model with $M_{\rm ZAMS} = {\rm XX}\ M_\odot$. For example, He15 and CO20 represent a helium star with $M_{\rm ZAMS} = 15\,M_\odot$ and a bare CO star with $M_{\rm ZAMS} = 20\,M_\odot$, respectively.

2.2. ^{56}Ni Mixing

During shock wave propagation, Rayleigh–Taylor and Richtmyer–Meshkov instabilities will develop, resulting in effective mixing of the ejecta (Kifonidis et al. 2003, 2006; Wongwathanarat et al. 2015). Such instabilities are important to the dynamics of the ejecta, but cannot be accurately modeled by 1D simulations. The effect of large-scale material mixing in the ejecta of CCSNe, with a focus on the radioactive energy source ^{56}Ni, have long been studied (Ensman & Woosley 1988; Shigeyama & Nomoto 1990; Shigeyama et al. 1990; Woosley & Weaver 1995; Sauer et al. 2006; Dessart et al. 2011, 2012; Bersten et al. 2013; Piro & Nakar 2013; Cano et al. 2014; Dessart et al. 2015, 2016; Yoon et al. 2019; Moriya et al. 2020; Teffs et al. 2020). However, the degree of mixing in the CCSN ejecta, and its possible dependence on the SNe progenitor, are difficult to constrain from observations. Based on the light curves of a large sample of SESNe from the Carnegie Supernova Project (CSP; Hamuy et al. 2006), Taddia et al. 2018 concluded that SNe IIb/Ib show variation in the degree of ^{56}Ni mixing, while for SNe Ic the ^{56}Ni is fully mixed into the ejecta with few exceptions. By studying the color curve evolution of SESNe, Yoon et al. (2019) also suggest that ^{56}Ni is only mildly mixed into the helium-rich layer of SNe IIb/Ib, while the ejecta of SNe Ic is fully mixed. This is further supported by the study of the evolution of the photospheric velocity at very early phases. Moriya et al. (2020) calculate the photospheric velocity evolution of SESNe with different degrees of ^{56}Ni mixing, and the models are further applied to an individual object, SN 2007Y. For this SN Ib, its photospheric velocity evolution matches well with the model where ^{56}Ni is only mixed into about half of the ejecta in mass coordinates.

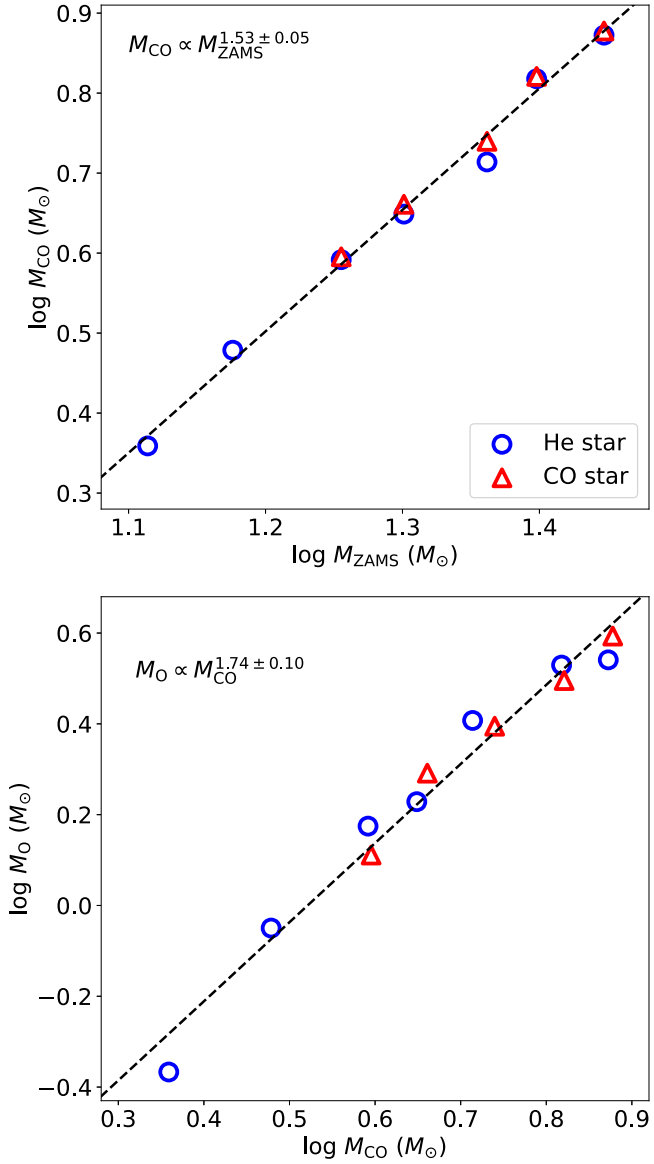

Figure 2. Upper panel: the relation between the CO core mass and the M_{ZAMS} of the progenitor models. Lower panel: the relation between the oxygen mass and the CO core mass.

^{56}Ni is an explosive-burning product, and its distribution is not strongly constrained by current models. In this work, ^{56}Ni is phenomenologically mixed with the method introduced as follow. First, 0.1 $M_\odot$ of ^{56}Ni is uniformly put in the innermost 10% (in mass coordinates) of the ejecta by hand. The ejecta are then artificially mixed by "boxcar" averaging (Kasen & Woosley 2009; Dessart et al. 2012, 2013; Morozova et al. 2015).[1] We define

$$f = \frac{X_{\rm Ni}(M_{\rm r} = 0.5 M_{\rm ejecta})}{X_{\rm Ni}(M_{\rm r} = 0)}, \quad (4)$$

i.e., the ratio of the ^{56}Ni fraction ($X_{\rm Ni}$) at the midpoint of the ejecta and that at the center of the ejecta. Here $M_{\rm r}$ is the mass coordinates after the remnant is excised. In this work, this ratio is employed to characterize the mixing degree of the ejecta. For each progenitor model, the degree of mixing f is varied from 0.1 to 1.0 ("fully mixed") with 0.1 increments by adjusting the width of the boxcar, as shown in the upper panel of Figure 3. The other elements in the ejecta are accordingly mixed by the boxcar averaging scheme. The ^{16}O distributions of the mixed

[1] The readers may refer to the notes of SNEC for details of this procedure.

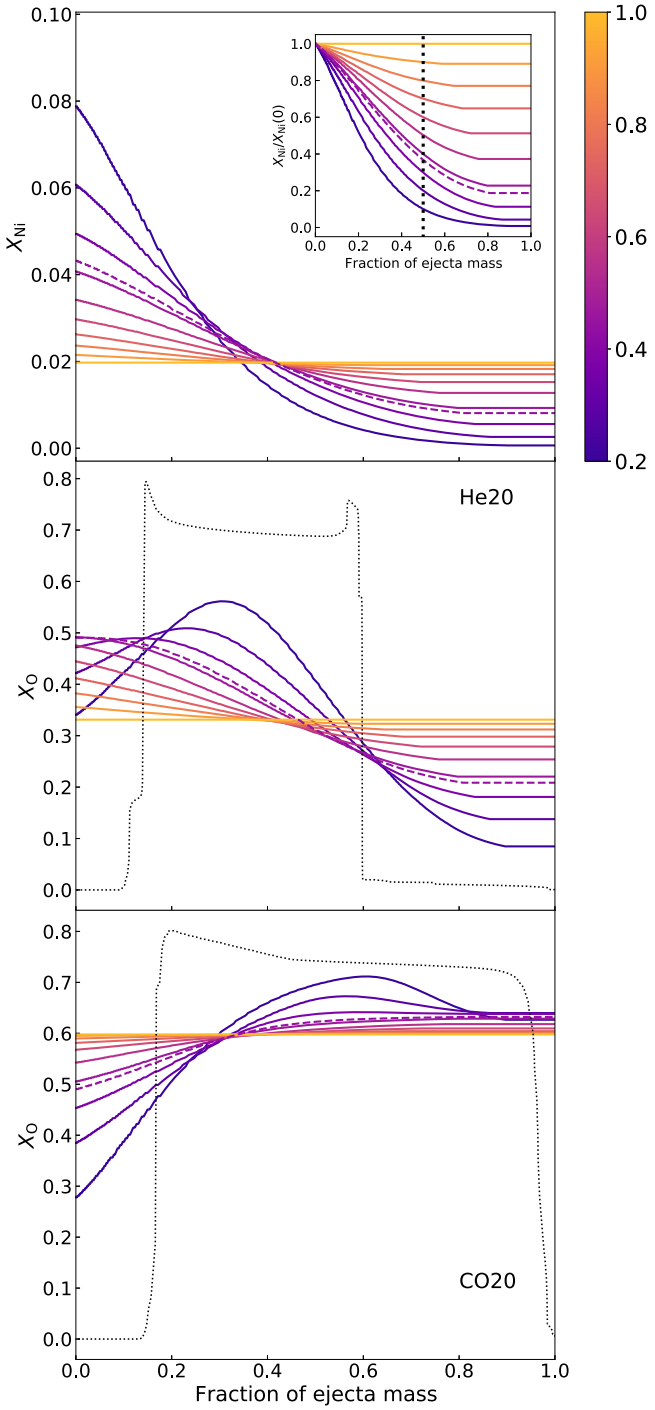

Figure 3. Upper panel: the ^{56}Ni mass fraction of the He20 model with different degrees of mixing, which is defined by Equation (4) and is labeled by different colors. The insert panel is the ^{56}Ni fraction divided by its maximum. The black dashed line marks the midpoint of the ejecta. Middle panel: the ^{16}O mass fraction of the He20 model with different degrees of mixing. The ^{16}O mass fraction of the preSN model (unmixed) is shown by the black dotted line for comparison. Lower panel: the ^{16}O mass fraction of the CO20 model with different degrees of mixing. The ^{16}O mass fraction of the preSN model is shown by the black dotted line for comparison.

ejecta with different f values are shown in the middle (He20 model) and lower panels (CO20 model) in Figure 3.

Yoon et al. (2019) characterized the ^{56}Ni distribution by

$$X_{\rm Ni}(M_{\rm r}) \propto \exp\left(-\left[\frac{M_{\rm r}}{f_{\rm Y19}M_{\rm ejecta}}\right]^2\right). \quad (5)$$

By studying the early phase color curve evolution of a sample of helium-rich SNe, Yoon et al. (2019) conclude that for these objects, ^{56}Ni is only mixed up to the midpoint of the helium-rich envelope, or $f_{\rm Y19} = 0.3$–0.5, which corresponds to $f = 0.368$ in the present work. Therefore, in the following analysis, we employ $f = 0.368$ as the default case, unless explicitly mentioned. The effect of large-scale mixing is discussed in Section 4.

2.3. SNEC: Explosion Hydrodynamics

Once the progenitor models have evolved to the time of CC, they are used as the input models of the hydrodynamics simulation of a SN explosion. In this work, we use SNEC (Morozova et al. 2015) to solve the hydrodynamic evolution of the SN ejecta.

Before the setup of the explosion, the materials are first mixed manually as introduced above. The explosion is initiated as the "thermal bomb" mode, i.e., the explosion energy is initially injected into a small mass range ($\Delta M = 0.1\,M_\odot$) and the injection lasts for 0.2 s. We vary the final energies (thermal energies plus kinetic energies) of the explosions ($E_{\rm K}$) from $\sim 10^{51}$ erg to 10×10^{51} erg with 0.5×10^{51} erg increments. In the following, we refer 10^{51} erg as 1 foe. The inner $1.4\,M_\odot$ is excised to account for the compact remnant formation.

The γ-ray deposition rates, as well as the density and velocity profiles of the ejecta ($t = 220$ days after the explosion) of the He18 and CO18 models with different kinetic energies, are plotted in Figure 4.

3. Connecting Models to Observables

3.1. Oxygen Mass and [O I]/[Ca II]

The [O I]/[Ca II] ratio is frequently employed as an indicator for the CO core mass of the progenitor. The oxygen mass is mainly determined by the progenitor CO core mass, to which the Ca mass is insensitive. However, the dependence of the [O I]/[Ca II] ratio on the O mass of the progenitor has not been quantitatively clarified from observations.

The SNe IIb spectral models of Jerkstrand et al. (2015) provide a possible constraint on the connection between the [O I]/[Ca II] ratio and the O mass of the ejecta. We apply the same method as Fang et al. (2022) to the model spectra to measure the [O I]/[Ca II] ratios, which are then compared with the O mass of the progenitor models in Jerkstrand et al. (2015), as shown in Figure 5. The average phase of the nebular SESNe in the sample of Fang et al. (2022) is 220 ± 80 days, therefore the measurements are limited to the model spectra at 150, 200, and 300 days. If we assume [O I]/[Ca II] $\propto M_{\rm O}^{\alpha}$, the linear regression in logarithmic scale gives $\alpha = 0.82$ (300 days) and

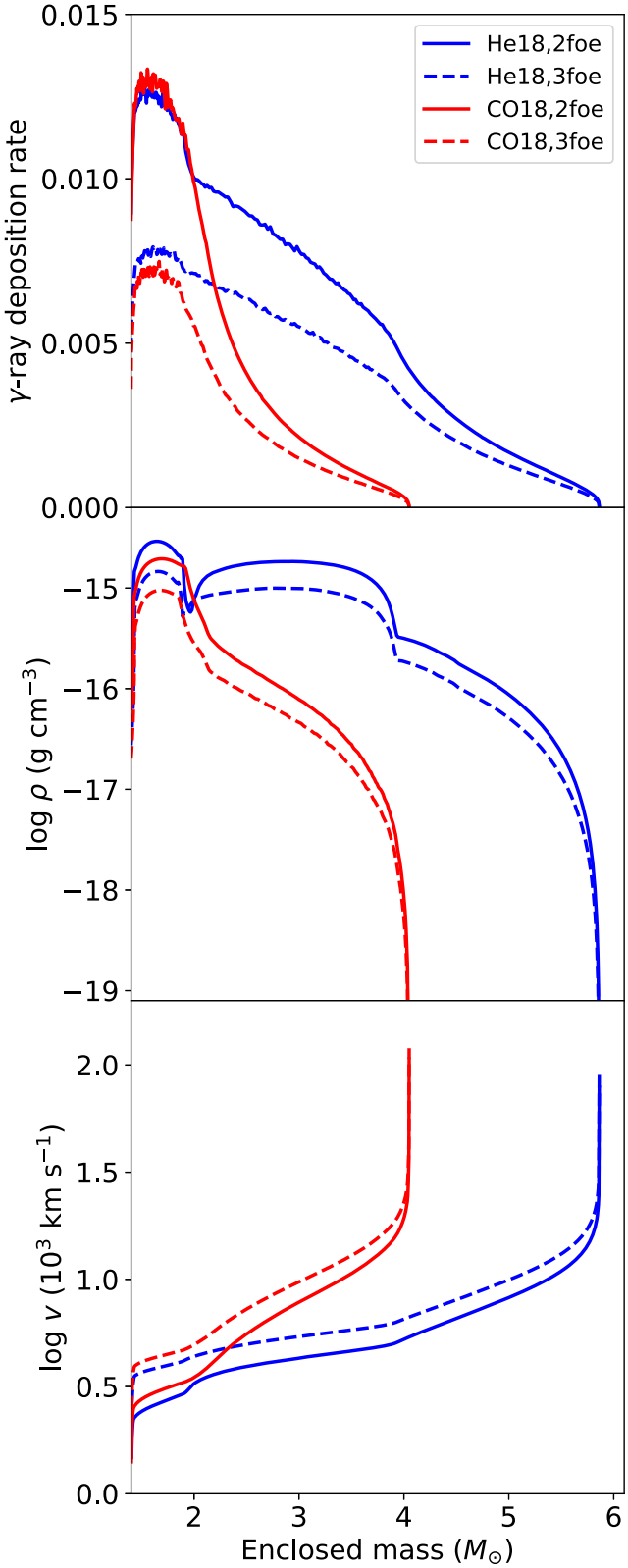

Figure 4. The physical properties of the ejecta of the He18 and CO18 models (labeled by different colors) with different kinetic energies (labeled by different line styles). Upper panel: the γ-ray deposition rate. Middle panel: the density profile. Lower panel: the velocity profile. These properties are shown for 220 days after the explosion.

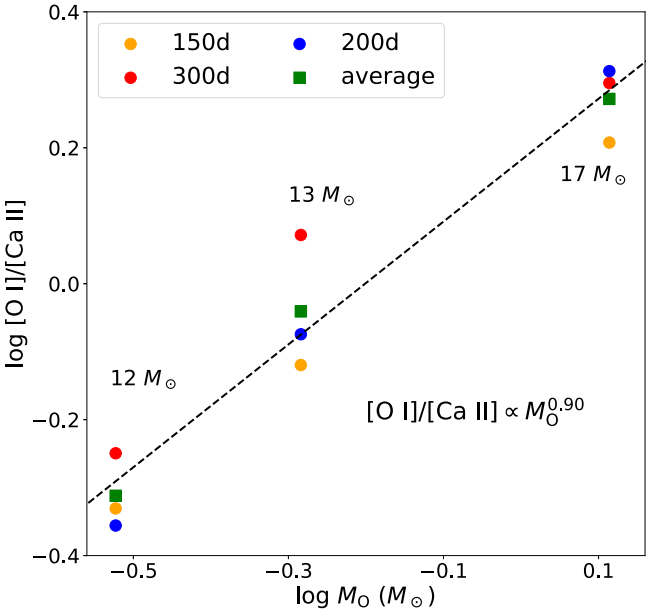

Figure 5. The relation between the [O I]/[Ca II] of SNe IIb model spectra (Jerkstrand et al. 2015) and the O mass of the ejecta. Measurements at different phases are labeled by different colors.

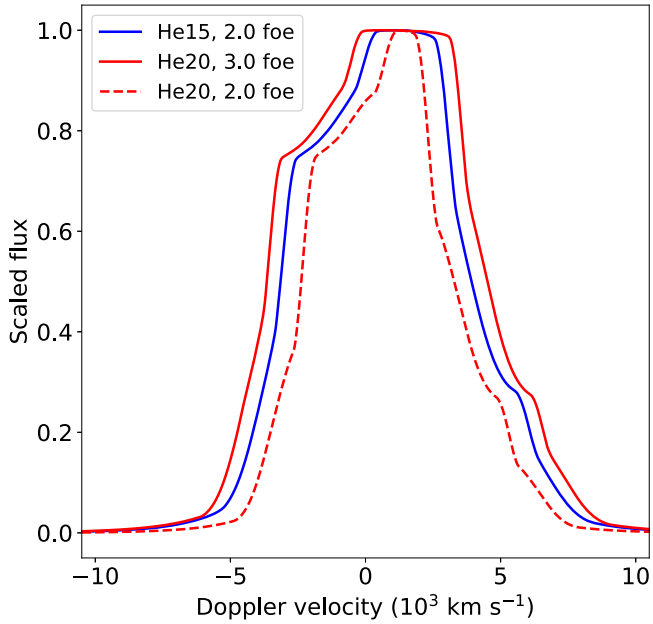

Figure 6. The line profiles constructed by Equations (7) and (8) for the He15 and He20 models (labeled by the different colors) with different kinetic energies (labeled by the different line styles).

1.01 (200 days). On average, we have

$$[\mathrm{O\,I}]/[\mathrm{Ca\,II}] \propto M_\mathrm{O}^{0.90\pm0.09}. \quad (6)$$

This relation will be applied to connect the [O I]/[Ca II] and the M_O of the helium star models in this work. Lacking consistent nebular model spectra of SNe Ic, whether this relation can be applied to the bare CO star models remains uncertain. While keeping this caveat in mind, it is illustrative to extend this relation to the helium-deficient models to compare with the observed SNe Ic/Ic-BL.

It should be noted that [O I]/[Ca II] is not only determined by the oxygen mass M_O, but is also affected by the physical properties of the ejecta, including the temperature, density, and so on. Here we have assumed that these quantities are ultimately determined only by the progenitor mass; therefore their effects on [O I]/[Ca II] are absorbed in the scaling index of M_O. Discussion on the variation form of Equation (6) is left to Section 4.1. We further note that we have fixed the metallicity in this investigation (assuming solar metallicity). The metallicity will introduce a mass-independent factor to the problem, but the observed variation of the metallicity at the SN site is not exceedingly large (see, for example, Modjaz et al. 2008); therefore its effect on the bulk statistics should be negligible.

3.2. Ejecta Velocity and [O I] width

The SN ejecta are powered by the deposited γ-rays originally emitted from the decay of ^{56}Ni and ^{56}Co, and the heating process is balanced by the line emission of the elements in each shell. In the expanding ejecta, each mass shell has a different expansion velocity; therefore the centers of the emission lines are Doppler shifted. In SNe, the Doppler effect is the dominating broadening factor of the lines; therefore the widths of the emission lines can inversely be utilized to determine the velocity scales of the corresponding emitting elements.

Following the explosion of a massive star, the ejecta expand homologously with $V(r, t) = r/t$, where $V(r, t)$ is the expansion velocity of the mass shell located at radius r at time t. In the spherically symmetric case, the specific flux at frequency ν is

$$F_\nu \propto \int_{V(\nu)}^{V_\mathrm{max}} j(V)VdV. \quad (7)$$

Here, V_max is the outermost velocity of the ejecta and $V(\nu) = \frac{\nu_0 - \nu}{\nu_0}c$, where ν_0 is the rest-frame frequency of the emission and c is the light speed. The emission coefficient in a mass shell with expansion velocity V is $j(V)$. The readers may refer to Jerkstrand (2017) for a detailed discussion on the formation of the nebular line profile.

The rate of radioactive energy deposited in a mass shell is $\epsilon_\mathrm{rad}d$ by definition, where d is the local γ-ray deposition function per mass. Here, ϵ_rad is the rate of energy release per gram of radioactive nickel. We assume that the deposited energy is reemitted by [O I] at a rate of $X_{\mathrm{O\ I}}\epsilon_\mathrm{rad}d$ (see below), where $X_{\mathrm{O\ I}}$ is the mass fraction of neutral oxygen. Therefore, we have

$$j_{[\mathrm{O\,i}]} \propto \rho X_{\mathrm{O\ I}}\epsilon_\mathrm{rad}d. \quad (8)$$

By assuming $X_{\mathrm{O\ I}} \sim X_\mathrm{O}$ and $L(6300)/L(6363) = 3$ (optically thin limit), the [O I] profile can be constructed by Equation (7). Some examples are illustrated in Figure 6.

Indeed, when oxygen dominates the cooling, its mass fraction would not sensitively affect the line strengths (i.e., the temperature is anyway determined to balance the heating and cooling rates). However, we introduce a factor X_O here, to account for the mixing effect as introduced above, since X_O traces the fraction of the O-rich material in a given volume once it is macroscopically mixed with other characteristic nuclear-burning layers. We note that we are not concerned with the absolute flux scale, and therefore this procedure is justified as long as X_O in the original (unmixed) ejecta are roughly constant within the O-rich region (which is indeed the case; Figure 1).

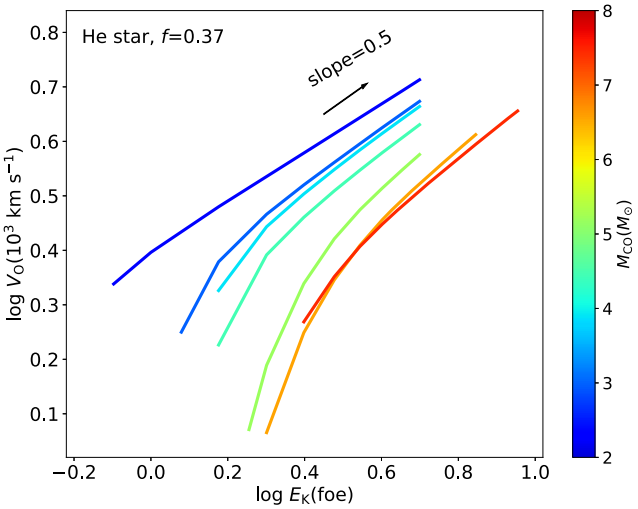

Figure 7. The relation between V_O and the E_K of the ejecta. The mixing degree f is fixed to be 0.368 to match with the results in Yoon et al. (2019). The color bar indicates M_{CO} of the progenitor. For a fixed M_{CO} (or progenitor model), the slope is very close to 0.5 in logarithmic scale at the relatively high E_K end.

We apply the same line width measurement method as Fang et al. (2022) to the model spectra, i.e., half of the wavelength range (or velocity range) that contains 68% of the total emission flux of the model [O I] profile. The measured line width is dependent on both M_O and E_K. As shown in Figure 7, for a fixed He star model (therefore fixed M_O), the measured width V_O scales as $V_O \propto E_K^{0.5}$.

3.3. [O I]/[Ca II]–[O I] Width Correlation

In Fang et al. (2022), a correlation between the [O I]/[Ca II] and [O I] width is discerned, based on a large sample of SESN nebular spectra ($N = 103$). For the helium-rich SNe IIb/Ib, the correlation is significant, while it is not clearly discerned for the helium-deficient SNe Ic/Ic-BL. The correlation itself, along with its different dependence on the SN subtypes, can be qualitatively explained if the kinetic energy of the explosion is correlated with the progenitor CO core mass. In this work, we will derive the quantitative relation between the CO core mass and the kinetic energy E_K that is required to reproduce the correlation.

First the observed line width $\Delta\lambda$ is transformed to the typical velocity scale V_{Obs} by

$$V_{Obs} = \frac{\Delta\lambda}{6300\ \text{Å}} \times c. \quad (9)$$

To connect the progenitor models to the observables, we assume [O I]/[Ca II] $\propto M_O^{0.90}$ (see Section 3.1). The oxygen mass M_O and the measured [O I] width V_O of the models are multiplied by constants to match the He13 model with $E_K = 0.94$ foe (see Fremling et al. 2016) with the [O I]/[Ca II] and V_{Obs} values of iPTF 13bvn. These calibrations give

$$\log \frac{[\text{O I}]}{[\text{Ca II}]} = 0.9 \times \log \frac{M_O}{M_\odot} + 0.03, \quad (10)$$

and

$$\log \frac{V_{Obs}}{10^3\ \text{km s}^{-1}} = \log \frac{V_O}{10^3\ \text{km s}^{-1}} - 0.07. \quad (11)$$

The upper panel of Figure 8 is the observational result of Fang et al. (2022). A local nonparametric regression is performed on the SNe IIb/Ib and SNe Ic/Ic-BL, respectively, as marked by the dashed lines. The shaded regions are the 95% confidence intervals (CIs). For a specific model, its M_O is transformed to the observed [O I]/[Ca II] using Equation (10). With the results from the local nonparametric regression, we derive V_{Obs} required for this progenitor model to reproduce the observed correlation, as marked in the upper panel of Figure 8, which is then further transformed to the model velocity (V_O)

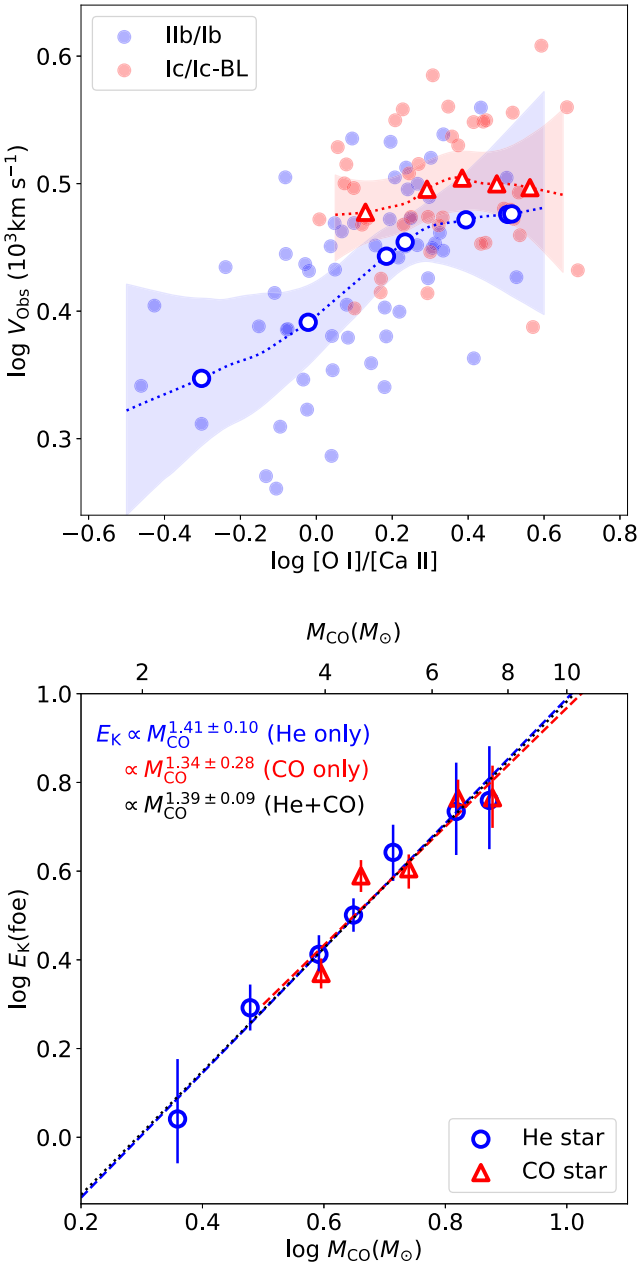

Figure 8. Upper panel: the observed [O I]/[Ca II]–[O I] width correlation. The helium-rich SNe (types IIb and Ib) and the helium-deficient SNe (types Ic and Ic-BL) are labeled by the different colors. The dashed lines are the local nonparametric regressions to the observations. The open circles and open triangles mark the helium star and CO star models, respectively. Lower panel: the relation between the CO core mass M_{CO} of the models and the kinetic energy required to produce the observed [O I]/[Ca II]–[O I] width correlation. The helium star and CO star models are labeled by the different colors and markers. The dashed lines are the linear regressions to the He star models (blue), CO star models (red), and He star + CO star models (black). The M_{CO}–E_K relations of the helium-rich and helium-deficient SNe are almost identical.

Table 2
The Kinetic Energy Required to Reproduce the Observed Correlation for the Progenitor Models

E_K (foe)	Lower	Middle	Upper
He13	0.88	1.10	1.49
He15	1.75	1.96	2.20
He18	2.38	2.58	2.84
He20	2.92	3.17	3.43
He23	3.81	4.39	5.03
He25	4.36	5.42	6.95
He28	4.49	5.75	7.57
CO18	2.18	2.34	2.51
CO20	3.60	3.88	4.19
CO23	3.66	4.03	4.31
CO25	5.36	5.82	6.36
CO28	5.02	5.83	6.84

Note. The upper and lower limits are transformed from the 95% CIs.

using Equation (11). The velocity, V_O, is transformed to the kinetic energy of the specific model using the relations in Figure 7. The results are summarized in Table 2.

It is clear that the kinetic energy of the explosion is required to be larger for the He star model with a larger amount of oxygen (therefore larger M_{ZAMS}) to produce the observed [O I]/[Ca II]–[O I] width correlation. This is already pointed out by the qualitative analysis of Fang et al. (2022). The relation between the CO mass (M_{CO}) and kinetic energy (E_K) is shown in the lower panel of Figure 8. If only the He star models are included, we have the scaling relation

$$E_K \propto M_{CO}^{1.41\pm0.10}. \quad (12)$$

If Equation (10) is also applied to the CO core models, with a similar practice, we derive the relation between the M_{CO} and E_K for these models, which is also plotted in the lower panel of Figure 8. For the CO core models, the scaling relation is

$$E_K \propto M_{CO}^{1.34\pm0.28}. \quad (13)$$

If the He star and the CO core models are combined, the relation between M_{CO} and E_K then becomes

$$E_K \propto M_{CO}^{1.39\pm0.09}, \quad (14)$$

which is similar to Equation (12) where only helium stars are included. The correlation is significant with a Spearman's rank coefficient of $\rho = 0.98$ and $p < 0.0001$. This implies the kinetic energies of SNe Ic have the same dependence on M_{CO} (or M_{ZAMS}) as their helium-rich counterparts, and possibly SNe IIb/Ib and SNe Ic share the same explosion mechanism despite the different degrees of the helium-rich layer stripping.

It should be noted that the scaling relation between the [O I]/[Ca II] ratio and M_O (Equation (6)) is empirically derived from the nebular helium-rich SNe models of Jerkstrand et al. (2015); therefore it is not necessarily valid for the helium-deficient SNe. The application of this relation to the CO core models and SNe Ic/Ic-BL is only for illustrative purpose. Further discussion on this topic is left to Section 4.1.

4. Discussion

4.1. Scaling Relation

4.1.1. Factors that Might Affect [O I]/[Ca II]

In the previous sections, we have assumed that [O I]/[Ca II] is determined only by the oxygen mass M_O, which is based on the assumption that other affecting factors (density, temperature, etc.) are also dependent on the progenitor mass so that their effects on [O I]/[Ca II] are all absorbed into the dependence on M_O. However, this assumption is not necessarily valid. The calcium emission [Ca II] comes from the explosive-nucleosynthesis region; therefore its strength may well be affected by the kinetic energy of the explosion. Further, calcium is an efficient coolant. If a certain amount of calcium (mass fraction larger than 10^{-3}) is microscopically mixed into the oxygen-rich shell through diffusion, the strength of [Ca II] will dominate [O I] and the [O I]/[Ca II] ratio will be reduced (Fransson & Chevalier 1989; Maeda et al. 2007; Dessart & Hillier 2020). These two factors, i.e., (1) the kinetic energy and (2) the microscopic mixing, will affect the [O I]/[Ca II] ratio as follows:

1. Kinetic energy: the kinetic energy will affect the [O I]/[Ca II] in two aspects: (1) the density of the ejecta. For the same preSN structure, an increase of the kinetic energy will increase the expansion velocity of the expelled material, resulting in low-density ejecta. The assumption that [O I] and [Ca II] dominate the emission from the O-rich shell and the explosive-nucleosynthesis region, respectively, is more valid when the density is lower. If the density of the O-rich shell increases, the contributions from Mg I] 4571 and [O I] 5577 become nonnegligible. For the explosive-nucleosynthesis region, the Ca II H&K near-infrared (NIR) triplet and Si I 1.099 μm become strong when the density of this region increases. However, the emission from the explosive-nucleosynthesis region is more sensitive to the density, therefore the decrease of the density (or increase of the explosion energy) will decrease the [O I]/[Ca II] ratio (Fransson & Chevalier 1989). (2) Nucleosynthesis: the amount of newly synthesized elements, including calcium, generally increases with the explosion energy (Woosley et al. 2002; Limongi & Chieffi 2003). The strength of [Ca II] thus traces the size of the explosive-nucleosynthesis region. An increase of the explosion energy will therefore decrease the [O I]/[Ca II] ratio.
2. Microscopic mixing: [Ca II] is mostly emitted by the newly synthesized calcium in the explosive-burning ash (Jerkstrand et al. 2015). Microscopic mixing is not expected to occur during the explosion because the diffusion timescale is long, as inferred from the chemical inhomogeneity of Cas A (Ennis et al. 2006). However, if the preexisting calcium, which is synthesized during the advanced stage of massive star evolution, is microscopically mixed into the O-rich shell before the explosion, its contribution to [Ca II] can become significant, and the [O I]/[Ca II] ratio will decrease because [Ca II] is a more effective coolant than [O I] (Dessart et al. 2021). Microscopic mixing may happen during the Si-burning stage through the merger of Si-rich and O-rich shells, and the occurrence rate is higher for a more massive

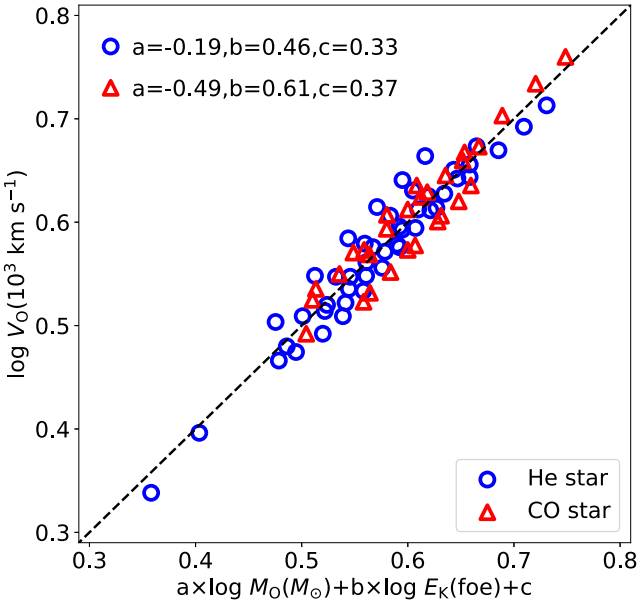

Figure 9. The linear regression to the model line width $V_O(M_O, E_K)$ as function of oxygen mass M_O and kinetic energy E_K. The helium star and the CO star models are labeled by the different colors and markers. The black dashed line is the one-to-one correspondence.

progenitor between 16 and 26 $M_\odot$ (Collins et al. 2018; Dessart & Hillier 2020).

In conclusion, both an increase of the kinetic energy E_K and the diffusion of calcium into the O-rich shell will tend to reduce the [O I]/[Ca II] ratio.

In Section 3, the derivation of the M_{CO}–E_K relation (Equation (14)) is based on the assumption that the [O I]/[Ca II] ratio is determined only by the oxygen content of the progenitor (Equation (10)). As stated above, this assumption is not necessarily valid. The relations between the [O I]/[Ca II] ratio and E_K, as well as the microscopic mixing, are complicated, and would possibly affect the M_{CO}–E_K relation. It is therefore important to examine how the M_{CO}–E_K relation is altered if the above two factors are taken into consideration. However, a detailed treatment on this topic would require a large grid of stellar evolution models and radioactive transfer simulations, which is beyond the scope of this paper. In this section, we attempt to quantify the effects of these two factors on the M_{CO}–E_K relation by including them into the scaling relation of the [O I]/[Ca II] ratio and M_O in power-law form. Equation (10) then becomes

$$\log \frac{[\mathrm{O\ I}]}{[\mathrm{Ca\ II}]} = (0.90 - \alpha) \times \log M_O - \beta \times \log E_K, \quad (15)$$

where α and β (both greater than 0) characterize the effects of microscopic mixing and the kinetic energy, respectively. Here, the effect of microscopic mixing is absorbed by the dependence on M_O because stellar evolution models show that the occurrence rate of shell mergers during the Si-burning stage is dependent on the progenitor mass, and more massive stars would have a higher chance of calcium pollution (Collins et al. 2018; Dessart & Hillier 2020).

4.1.2. M_{CO}–E_K Relation of SNe IIb/Ib

To examine the effects of E_K and microscopic mixing on the M_{CO}–E_K relation, we first need to derive the scaling relations between the observables and the models. For the He star models with $f = 0.368$, the measured line width is determined by M_O and E_K, and the linear regression gives

$$\log \frac{V_O}{10^3\ \mathrm{km\ s^{-1}}} = (-0.20 \pm 0.01) \times \log \frac{M_O}{M_\odot} + (0.46 \pm 0.02) \times \log \frac{E_K}{\mathrm{foe}} + (0.33 \pm 0.01), \quad (16)$$

as shown in Figure 9.

The relation between the observed line width V_{obs} and the [O I]/[Ca II] can also be expressed in the form of a power law derived from the linear regression in logarithm scale

$$\log \frac{V_{Obs}}{10^3\ \mathrm{km\ s^{-1}}} = (0.18 \pm 0.04) \times \log \frac{[\mathrm{O\ I}]}{[\mathrm{Ca\ II}]} + 0.41 \pm 0.01. \quad (17)$$

By combining Equations (3), (15), (16), and (17), we have $E_K \propto M_{CO}^{\delta}$ (including α and β as unknown parameters), where

$$\delta = \frac{0.63 - 0.31\alpha}{0.46 + 0.18\beta}. \quad (18)$$

If $\alpha, \beta = 0$ (in this case, Equation (15) recovers Equation (10), where [O I]/[Ca II] $\propto M_O^{0.9}$), then $\delta = 1.37$, which is similar to Equation (12) as expected. With Equation (18), we can investigate how the scaling index δ of the M_{CO}–E_K relation is affected by the effects of E_K and the microscopic mixing (characterized by the parameters β and α, respectively).

We first consider the effect of E_K on the [O I]/[Ca II] ratio. In the nebular models of Fransson & Chevalier (1989), [O I]/[Ca II] scales as $E_K^{-0.5}$. In this case ($\beta = 0.5$ and $\alpha = 0$), we have $\delta = 1.14$. Still, this would require E_K to be tightly correlated with M_{CO}, although the dependence is slightly weaker than in Equation (12).

Lacking a large grid of nebular spectra models with different degrees of microscopic mixing, it is difficult to derive the exact value of α. However, its range can be roughly constrained from observations. If α is larger than 0.9, then according to Equation (15), the [O I]/[Ca II] ratio will be anticorrelated with the progenitor oxygen mass M_O. However, Fang et al. (2019) find a correlation between the [O I]/[Ca II] ratio and the light-curve width. The light-curve width measures the diffusion timescales of the photons, which is an independent measurement of the ejecta mass (as a representation of the progenitor mass). This correlation is justified by Karamehmetoglu et al. (2022): their sample of SESNe with broad light curves have distinctly larger [O I]/[Ca II]. The [O I]/[Ca II] ratio is not heavily affected by microscopic mixing (otherwise this correlation would not be expected), but the oxygen content in the ejecta should be the dominant factor, with larger [O I]/[Ca II] implying a more massive CO core.

Although the degree of preSN calcium pollution is difficult to be inferred from current observations, its effect on [O I]/[Ca II] is probably not very strong, and α cannot be too large, or at least should be smaller than 0.9. With this constraint, $\delta > 0.76$ if $\beta = 0$, according to Equation (18).

In the most extreme case where $\alpha = 0.9$ and $\beta = 0.5$, we have $\delta = 0.64$. In conclusion, even when the effects of kinetic energy and calcium pollution are taken into account, we would still expect a positive correlation between $E_{\rm K}$ and $M_{\rm CO}$ to explain the observed correlation in Figure 8. However, to derive the exact relation between $E_{\rm K}$ and $M_{\rm CO}$ based on the correlation between [O I]/[Ca II] and [O I] width, sophisticated models that can constrain both α and β are needed.

4.1.3. M_{CO}–E_K Relation of SNe Ic/Ic-BL

Similar to the practice in the previous section, for the CO star models, the relation between the model line width $V_{\rm O}$, kinetic energy $E_{\rm K}$, and model oxygen mass $M_{\rm O}$ is given by

$$\log \frac{V_{\rm O}}{10^3\ {\rm km\ s^{-1}}} = (-0.49 \pm 0.05) \times \log \frac{M_{\rm O}}{M_\odot} + (0.61 \pm 0.04) \times \log \frac{E_{\rm K}}{\rm foe} + (0.37 \pm 0.02), \quad (19)$$

as shown in Figure 9. Also, the relation between the observed line width $V_{\rm Obs}$ and the [O I]/[Ca II] ratio is given by

$$\log \frac{V_{\rm Obs}}{10^3\ {\rm km\ s^{-1}}} = (0.04 \pm 0.05) \times \log \frac{\rm [O\ I]}{\rm [Ca\ II]} + 0.48 \pm 0.02. \quad (20)$$

For SNe Ic and Ic-BL, the combination of Equations (3), (15), (19), and (20) gives

$$\delta = \frac{0.89 - 0.07\alpha}{0.61 + 0.04\beta}. \quad (21)$$

If α, $\beta = 0$ and $\delta = 1.46$, which are consistent with Equation (13) as expected. Unlike the helium-rich SNe, the effects of kinetic energy (β) and the level of microscopic mixing (α) on δ is very weak. In the most extreme case where $\alpha = 0.9$ and $\beta = 0.5$, we still have $\delta = 1.31$.

The derivation of Equation (21) is based on the assumption that the CO star models follow the same $M_{\rm O}$–[O I]/[Ca II] scaling relation as the helium star models (Equation (10) or (15)). However, as noted above, these relations are not necessarily valid for the CO star models. Observationally, for SNe Ic/Ic-BL, the dependence of the [O I] width on [O I]/[Ca II] is weak. By applying Equations (3) and (19) with $V_{\rm O}$ fixed to be a constant (Figure 8) and α, $\beta = 0$, we have

$$E_{\rm K} \propto M_{\rm CO}^{1.40}. \quad (22)$$

For the helium-deficient SNe, although currently we lack consistent SNe Ic nebular spectra models to constrain the relation between $M_{\rm O}$ and [O I]/[Ca II], the power index δ derived from the simple scaling analysis (Equation (22)) is consistent with that of the helium-rich models, which again suggests that SESNe share the same explosion mechanism.

4.2. Effect of Macroscopic Mixing

Large-scale material mixing (macroscopic mixing) in CCSN ejecta would occur due to the instabilities which likely arise during the explosion. Instabilities are expected to take place at the interface between the CO core and the He-rich layer, bring up material from the CO core to the outer region. If ^{56}Ni and oxygen are mixed into the outer region (therefore with faster expansion velocities according to the assumption of homologous expansion), the line widths will increase based on Equation (7). In particular, the mixing of the radioactive ^{56}Ni strongly affects the electromagnetic properties and the thermal conditions. The line width is therefore affected by the interplay of these factors, even if the preexplosion structure and the kinetic energy $E_{\rm K}$ are fixed. In this section we will investigate whether the degree of mixing can account for the observed large scatter in the [O I] width and affect the $M_{\rm CO}$–$E_{\rm K}$ relation.

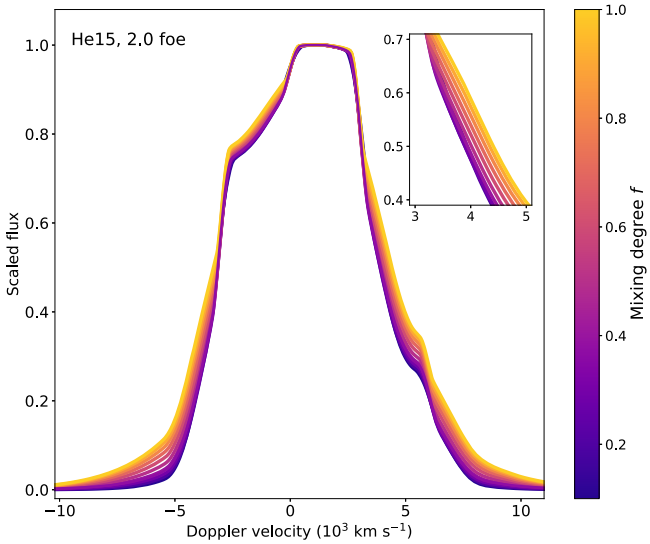

Figure 10. The [O I] profiles of the He15 model ($E_{\rm K} = 2.0$ foe) with different degrees of macroscopic mixing, labeled by the color bar.

Using the mixing scheme introduced in Section 2.2, we artificially vary the degree of mixing f from 0.1 to 1.0 (being fully mixed), and calculate the [O I] profiles for different progenitor models with different kinetic energies. The [O I] profiles of the He15 model ($E_{\rm K} = 2.0$ foe) calculated with different f values are shown in Figure 10 as examples. An increase of f indeed leads to a larger line width. To investigate the effect of f on the observed line width, we calculate $V_{\rm Obs}$ for each of the progenitor model with f varied and the $M_{\rm CO}$–$E_{\rm K}$ relation kept fixed (Table 2). The expected [O I]/[Ca II]–[O I] width relations are shown in Figure 11 for different f values. For the same explosion of the same He-rich progenitor, the different degrees of large-scale material mixing indeed create the scatter in the line width, and can fully account for the observed scatter (the blue shaded region in Figure 11). However, for the CO star models, the effect of large-scale mixing on the line width is negligible. Unlike the He star models, where the material in the CO core are dredged up to the outer region, for the CO star models, the mixing process will bring the O-rich material down to the inner region and the average velocity is reduced (lower panel in Figure 3). This effect is canceled out with the dredge up of the radioactive ^{56}Ni.

By studying the color evolution of early phase light curves, Yoon et al. (2019) find evidence that the ejecta of SNe Ic are fully mixed, while for SNe IIb/Ib, the radiative ^{56}Ni is only mildly mixed into the helium-rich envelope. This is also supported by the study of early photospheric velocity evolution: Moriya et al. (2020) find the helium star model can explain the photospheric velocity evolution of type Ib SN 2007Y, if the mixing process penetrates up to the middle of the ejecta. These investigations suggest that the degree of mixing is

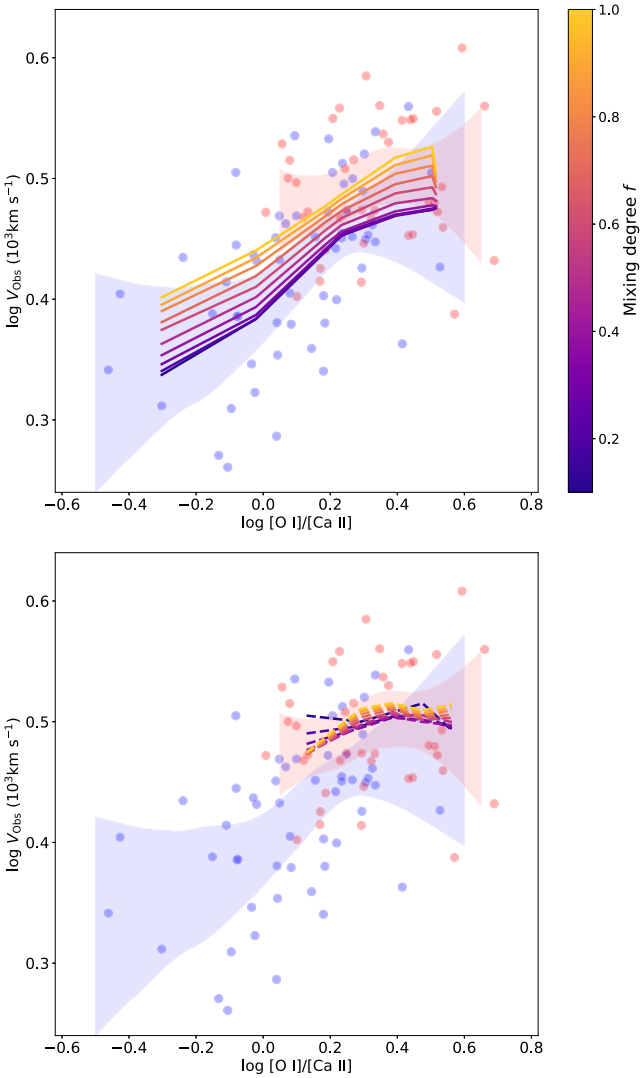

Figure 11. The [O I]/[Ca II] line width tracks of models with different degrees of macroscopic mixing (labeled by the color bar) while the $M_{\rm CO}$–$E_{\rm K}$ relation is fixed (Table 2). The observed [O I]/[Ca II]–[O I] width relations of SNe IIb/Ib and SNe Ic/Ic-BL are illustrated as the shaded regions for comparison. Upper panel: the tracks of the He star models are labeled by the solid lines. Lower panel: the tracks of the CO star models are labeled by the dashed lines.

possibly related to the properties of the progenitor. In this work, we have assumed that the models have the same degree of mixing ($f = 0.368$). If f is mass dependent, for example, in the case where more massive progenitors would lead to a larger value of f, the required kinetic energy will decrease to reproduce the fixed observed velocity; this reduces the slope in Equation (14). We further investigate whether the change of the degree of mixing f will affect the $M_{\rm CO}$–$E_{\rm K}$ relation.

Similarly to the process in Section 3.3, we derived $E_{\rm K}$ for each progenitor model with different degrees of macroscopic mixing f based on the observed line width. We consider two cases: (1) f is positively correlated with progenitor mass, i.e., the ejecta of a more massive star are more thoroughly mixed, with $f = 0.1$ for the He13 model and $f = 1.0$ for the He28 model; and (2) f is anticorrelated with progenitor mass, with $f = 1.0$ for the He13 model and $f = 0.1$ for the He28 model. The results are shown in Figure 12, with models with different f labeled by the color bar. For case (1), we have $E_{\rm K} \propto M_{\rm CO}^{1.26}$. For case (2), the dependency increases to $E_{\rm K} \propto M_{\rm CO}^{1.58}$, as illustrated

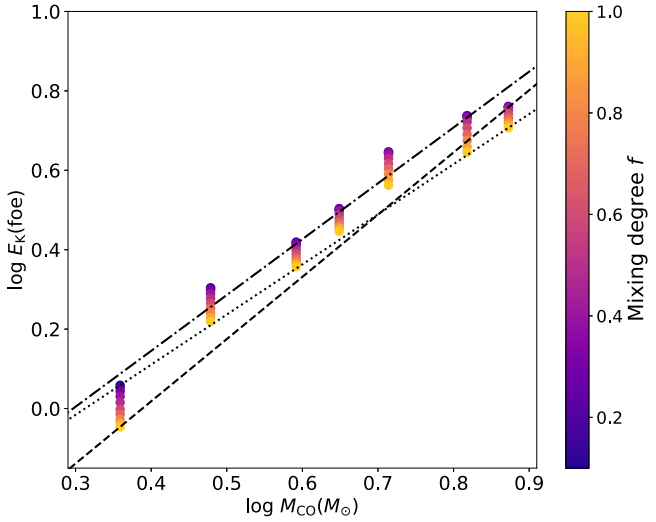

Figure 12. The $M_{\rm CO}$–$E_{\rm K}$ relation required to produce the observed [O I][Ca II]–line width relation for the helium star models with different degrees of macroscopic mixing, labeled by the color bar. The dashed line is the $M_{\rm CO}$–$E_{\rm K}$ relation if the mixing degree f is anticorrelated with the progenitor mass; the dotted line is the $M_{\rm CO}$–$E_{\rm K}$ relation if the mixing degree f is correlated with the progenitor mass. The dotted–dashed line is the $M_{\rm CO}$–$E_{\rm K}$ relation with f fixed to 0.368 (lower panel of Figure 8) for comparison.

by the dotted line and dashed line in Figure 12, respectively. In conclusion, even the relation between the mixing degree and the progenitor is unknown with our current knowledge, and the $M_{\rm CO}$–$E_{\rm K}$ relation will not be significantly affected.

5. Comparison with Early Phase Observations

The relation between the properties of the progenitor and the kinetic energy has long been studied. However, most of the previous investigations focused on early phase (or photospheric phase) observations (Lyman et al. 2016; Taddia et al. 2018). The width of the light curve and the photospheric velocity estimated from early phase spectra are used to derive the mass of the ejecta and the kinetic energy of the explosion, based on the model of Arnett (1982), where the ejecta are predominantly powered by the decay of radioactive ^{56}Ni and ^{56}Co.

During the photospheric phase, the ejecta are optically thick. Instead of scanning through the ejecta, the information brought by analyzing the early phase observational data is limited to the properties of the outer region. The bulk properties of the ejecta are then estimated from the extrapolation inward based on several simplified assumptions (Arnett 1982; Valenti et al. 2008; Cano 2013; Lyman et al. 2016; Taddia et al. 2018). The observations at the photospheric phase and nebular phase are indeed tracing different regions of the ejecta; therefore it is important to compare the results derived from the two observations to clarify the validity of the assumptions.

The first step in the investigation on this topic is to connect the early phase/nebular phase observables with the models. In this section, we employ the results of Lyman et al. (2016) and Taddia et al. (2018), which derive the ejecta mass $M_{\rm ejecta}$ and the kinetic energy $E_{\rm K}$ from early phase multiband light curves of large samples of SESNe, based on the Arnett model and radiation hydrodynamic models, respectively.

The ejecta mass estimated from the early phase observables are transformed to the preSN mass by

$$M_{\rm pre-SN} = M_{\rm ejecta} + 1.4 M_\odot, \quad (23)$$

assuming that the remnant of the explosion is fixed to $1.4\,M_\odot$. For the He star models, the preSN mass is further transformed to the CO core mass $M_{\rm CO}$ by

$$\log \frac{M_{\rm CO}}{M_\odot} = (1.245 \pm 0.008) \times \log \frac{M_{\rm pre-SN}}{M_\odot} - 0.366 \pm 0.006. \quad (24)$$

Similarly, for the CO core models, we have

$$\log \frac{M_{\rm CO}}{M_\odot} = (1.013 \pm 0.008) \times \log \frac{M_{\rm pre-SN}}{M_\odot} - 0.018 \pm 0.006. \quad (25)$$

We first anchor the absolute scale of the ejecta mass from the early phase analysis of Lyman et al. (2016). The ejecta mass of iPTF 13bvn derived from the Arnett model is multiplied by a constant to match with the He13 model, which gives

$$\log \frac{M_{\rm ejecta,\ model}}{M_\odot} = \log \frac{M_{\rm ejecta,\ LC}}{M_\odot} + 0.15. \quad (26)$$

Here, $M_{\rm ejecta,model}$ and $M_{\rm ejecta,LC}$ are the ejecta mass of the progenitor model and the ejecta mass estimated from the early phase light curve, respectively. For the sample of Taddia et al. (2018), we directly apply their $M_{\rm ejecta}$, as it was estimated based on radiation hydrodynamic simulations. The ejecta mass is further transformed to the CO core mass using Equations (23), (24), (25), and (26). The $M_{\rm CO}$ values are then compared with the kinetic energies derived from the early phase light curve.

The $M_{\rm CO}$–$E_{\rm K}$ relations based on the early phase analyses from Lyman et al. (2016) and Taddia et al. (2018) are plotted in the upper and lower panels of Figure 13, respectively. The helium-rich SNe (IIb and Ib) and the helium-deficient SNe (Ic and Ic-BL) are labeled by the different colors and markers. The $M_{\rm CO}$–$E_{\rm K}$ relation derived from the nebular spectra (lower panel of Figure 8) is also plotted for comparison.

5.1. Comparison with Lyman et al. (2016)

$M_{\rm ejecta}$ and $E_{\rm K}$ of the Lyman et al. (2016) sample are derived based on the Arnett model with several simplified assumptions, for which the readers may refer to Arnett (1982) and Lyman et al. (2016) for more details.

For the Lyman et al. (2016) sample, the linear regressions to SNe IIb and Ib and SNe Ic and Ic-BL give

$$E_{\rm K} \propto M_{\rm CO}^{1.31\pm0.18}, \quad (27)$$

and

$$E_{\rm K} \propto M_{\rm CO}^{1.18\pm0.33}, \quad (28)$$

respectively. If the linear regression is performed on the full sample, we have

$$E_{\rm K} \propto M_{\rm CO}^{1.36\pm0.16}. \quad (29)$$

The slope of the $M_{\rm CO}$–$E_{\rm K}$ relation of the SNe IIb and Ib is consistent with the one derived from the nebular phase observations. The consistency between the analyses using the early phase and nebular phase observables further suggests the effects of $E_{\rm K}$ and the degree of microscopic mixing on [O I]/[Ca II] is probably not very strong. To be more specific, we now look into Equation (18). To match with the result from the nebular phase observations, with $\delta = 1.31$ derived from the early phase observations, the values of α and β are constrained by

$$0.31\alpha + 0.24\beta = 0.03, \quad (30)$$

therefore $\alpha < 0.10$ and $\beta < 0.13$ (α, $\beta > 0$; see the discussion in Section 4.1).

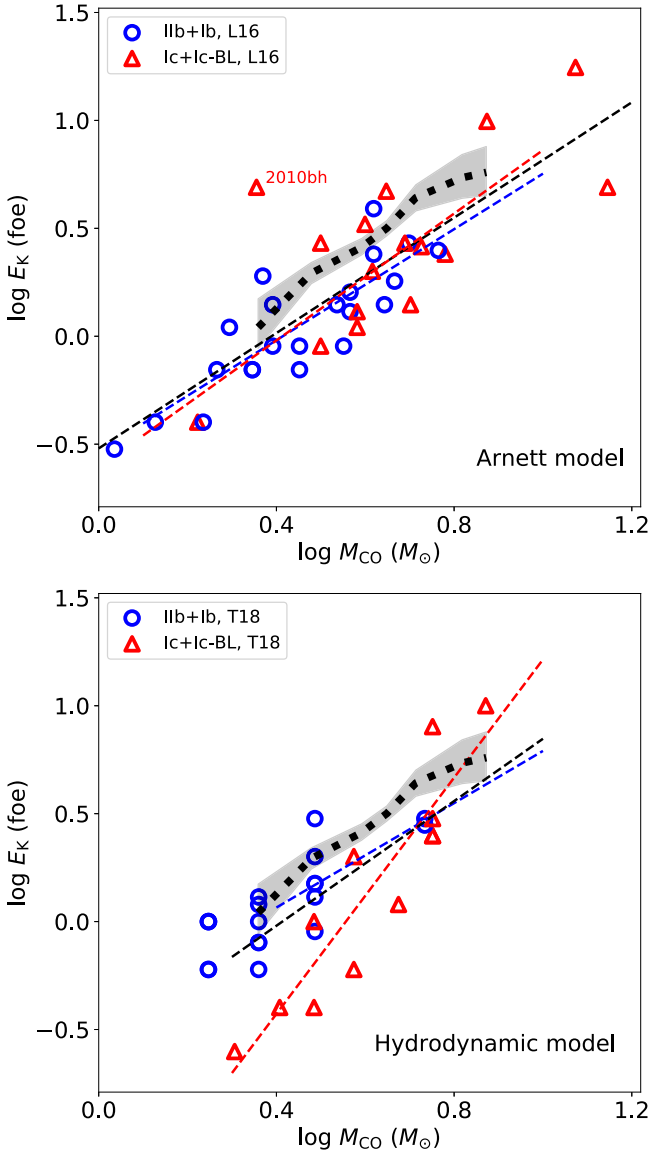

Figure 13. The $M_{\rm CO}$–$E_{\rm K}$ relation derived using the early phase observables. The scatter points are individual objects, with SNe IIb and Ib labeled by blue circles and SNe Ic and Ic-BL labeled by red triangles. The blue and red dashed lines are the linear regressions to the helium-rich and helium-deficient SNe, respectively. The black dashed lines are the linear regressions to the full sample. The black dotted line is the result derived from the nebular spectrum analysis, with the shaded area showing the 95% confidence level (lower panel of Figure 8). Upper panel: the relation based on the early phase observations from Lyman et al. (2016), with $M_{\rm ejecta}$ and $E_{\rm K}$ estimated from the Arnett model. Lower panel: the relation based on Taddia et al. (2018), with $M_{\rm ejecta}$ and $E_{\rm K}$ estimated from the hydrodynamic models.

For the He-deficient SNe, the power-law index δ derived from the early phase observations is smaller than the one derived from the nebular phase observations (Equation (22)), but still the two relations are consistent within their uncertainties. Further, if the possible outlier SN 2010bh is excluded (as labeled in the upper panel of Figure 13), the linear regression gives

$$E_{\rm K} \propto M_{\rm CO}^{1.47\pm0.29}. \quad (31)$$

In conclusion, for SNe IIb/Ib and SNe Ic/Ic-BL, the $M_{\rm CO}$–$E_{\rm K}$ relations from both the early phase and nebular phase observations are consistent.

5.2. Comparison with Taddia et al. (2018)

Instead of using the Arnett model, $M_{\rm ejecta}$ and $E_{\rm K}$ of the Taddia et al. (2018) sample are derived based on a radiation hydrodynamic model. The light curves of the SNe in the sample are compared with the simulated light curves, which are generated by exploding a series of helium star models with different progenitor masses using a range of kinetic energies. The ejecta masses $M_{\rm ejecta}$ of the Taddia et al. (2018) sample are transformed to CO core masses $M_{\rm CO}$ via Equations (23), (24), and (25).

The linear regressions to the SNe IIb and Ib and SNe Ic and Ic-BL of the Taddia et al. (2018) sample give

$$E_{\rm K} \propto M_{\rm CO}^{1.23\pm0.22}, \quad (32)$$

and

$$E_{\rm K} \propto M_{\rm CO}^{2.74\pm0.39}, \quad (33)$$

respectively. The $M_{\rm CO}$–$E_{\rm K}$ relation of the SNe IIb/Ib derived based on early phase observations is consistent with the one from the nebular phase observations within their uncertainties. Similar to the analysis of the Lyman et al. (2016) sample, Equation (32) constrains the values of α and β through

$$0.31\alpha + 0.22\beta = 0.06, \quad (34)$$

and $\alpha < 0.21$ and $\beta < 0.29$, i.e., the effects of $E_{\rm K}$ and microscopic mixing on [O I]/[Ca II] are negligible, which is similar with the case of the Lyman et al. (2016) sample.

However, for the SNe Ic/Ic-BL sample, the slope of Equation (33) is much larger than the ones derived from the nebular analysis (Equation (13)) and the sample of Lyman et al. (2016). This is possibly because Taddia et al. (2018) estimate the $E_{\rm K}$ and $M_{\rm ejecta}$ of the helium-deficient SNe by comparing their observed light curves with simulated light curves of helium-rich star models. This potentially introduces a systematic offset in $E_{\rm K}$ and $M_{\rm ejecta}$, which in turn affects the slope of Equation (33).

6. Summary

Based on a large nebular spectra sample of SESNe, Fang et al. (2022) found a correlation between [O I]/[Ca II] (which measures the progenitor mass) and [O I] width (which measures the expansion velocity of the O-rich material). This work aims to explain this correlation from a theoretical aspect.

One-dimensional simulations of massive star evolution from 13 to 28 $M_\odot$, with the hydrogen envelope or the helium-rich layer stripped, are carried out using MESA. When the massive stars evolve to the time of CC, they are used as input models for SNEC, and further exploded as CCSNe by injecting different amounts of kinetic energy ($1–10\times10^{51}$ erg) into the central regions. The oxygen mass of each model is transformed to the [O I]/[Ca II] ratio by assuming the scaling relation derived from the nebular SN IIb models of Jerkstrand et al. (2015). The velocity of the O-rich materials as weighted by the local γ-ray deposition rate is connected to the observed [O I] width. The analysis in this work suggests the following to produce the correlation between the [O I]/[Ca II] ratio and the [O I] width: the kinetic energy of the explosion should correlate with the CO core mass of the ejecta, and scales as $E_{\rm K} \propto M_{\rm CO}^{1.41}$. Further, SNe Ic/Ic-BL follow almost the same $M_{\rm CO}$–$E_{\rm K}$ relation as SNe IIb/Ib, i.e., $E_{\rm K} \propto M_{\rm CO}^{1.34}$, which suggests that helium-rich and helium-deficient SNe likely share the same explosion mechanism.

However, the above inferences are made based on several simplified assumptions and empirical relations (for example, we adopt a specific model sequence for SNe IIb by Jerkstrand et al. 2015 for the conversion between the [O I]/[Ca II] ratio and $M_{\rm O}$). Lacking consistent nebular model spectra of SESNe exploded by a large range of the kinetic energies, it is difficult to estimate the accuracy of the $M_{\rm CO}$–$E_{\rm K}$ relation derived from the method presented in this work. We have discussed several factors that would possibly affect the result. With the scaling analysis, we conclude that the power-law index of the $M_{\rm CO}$–$E_{\rm K}$ relation of the helium-rich SNe is affected by the dependence of the [O I]/[Ca II] ratio on $E_{\rm K}$ and the degree of microscopic mixing. However, the power-law index of the $M_{\rm CO}$–$E_{\rm K}$ relation is insensitive to such dependence, especially for the helium-deficient SNe. Further, the macroscopic mixing potentially developed during the explosion will bring material in the CO core up to outer region, increasing the average velocity of the O-rich material and the [O I] width. Different degrees of macroscopic mixing can create the scatter in the observed line widths.

The derivation of an accurate $M_{\rm CO}$–$E_{\rm K}$ relation is associated with these complicated physical issues, and therefore would require a large grid of detailed radiative transfer modeling with the above factors taken into account. Sophisticated stellar evolution modeling is also needed to estimate the occurrence rate of the microscopic mixing of calcium into the O-rich shell, which is caused by shell mergers developing during the advanced nuclear-burning stage.

With the above caveats in mind, we compare the $M_{\rm CO}$–$E_{\rm K}$ relation derived from this work with the early phase observations of Lyman et al. (2016) and Taddia et al. (2018). During the early phase, the ejecta are optically thick, and the observations trace the nature of the outer region. When the ejecta enter nebular phase, they becomes transparent, and the observations probe the nature of the densest region, i.e., the innermost part. The observations at different phases are thus independently constraining the natures of different regions within the ejecta. Interestingly, for the helium-rich SNe, the $M_{\rm CO}$–$E_{\rm K}$ relation derived from these two methods are in good agreement. It is largely the case for the helium-deficient SNe as well, but the situation is less clear; while the scaling we have derived for the core region agrees with the one derived from the outer region by Lyman et al. (2016), the power-law index of the $M_{\rm CO}$–$E_{\rm K}$ derived from the sample of Taddia et al. (2018) is too steep compared with the nebular phase observations. This is possibly because the analysis of the SNe Ic/Ic-BL in the sample of Taddia et al. (2018) is based on helium-rich models. We emphasize that the $M_{\rm CO}$–$E_{\rm K}$ relations derived for the outer

region (by the early phase analysis) and for the innermost region (by the late phase analysis) do not have to agree, as different regions are being probed.

In this work, we present a method to investigate the relation between the progenitor mass and the kinetic energy of the explosion through nebular phase observations. Although this method suffers from a lack of consistent nebular spectra models, it can serve as a cross-reference of the ejecta properties inferred from the early phase observations, which were frequently adopted in the previous literature. The combined analysis of the observational data in the early and late phases provides us with the chance to scan through the full ejecta from the outermost region to the dense inner part. Not only the consistency, but also the inconsistency of the two methods, are important to investigate the completeness of the current assumptions on the explosion process, which are crucial to reveal the explosion mechanism of CCSNe.

The authors would like to thank the anonymous reviewer for the comments that helped to improve the manuscript. Q.F. acknowledges support by the Japan Society for the Promotion of Science (JSPS) KAKENHI Grant (20J23342). K.M. acknowledges support by JSPS KAKENHI Grants (18H05223, 20H00174, and 20H04737).

Software: MESA (Paxton et al. 2011, 2013, 2015, 2018, 2019); SNEC (Morozova et al. 2015); SciPy (Virtanen et al. 2020); NumPy (Harris et al. 2020); Astropy (Astropy Collaboration et al. 2013, 2018); Matplotlib (Hunter 2007).

ORCID iDs

Qiliang Fang (方其亮) https://orcid.org/0000-0002-1161-9592
Keiichi Maeda https://orcid.org/0000-0003-2611-7269

References

Arnett, W. D. 1982, ApJ, 253, 785
Astropy Collaboration, Price-Whelan, A. M., Sipőcz, B. M., et al. 2018, AJ, 156, 123
Astropy Collaboration, Robitaille, T. P., Tollerud, E. J., et al. 2013, A&A, 558, A33
Bersten, M. C., Benvenuto, O. G., Folatelli, G., et al. 2014, AJ, 148, 68
Bersten, M. C., Tanaka, M., Tominaga, N., et al. 2013, ApJ, 767, 143
Cano, Z. 2013, MNRAS, 434, 1098
Cano, Z., Maeda, K., & Schulze, S. 2014, MNRAS, 438, 2924
Cao, Y., Kasliwal, M. M., Arcavi, I., et al. 2013, ApJL, 775, L7
Collins, C., Müller, B., & Heger, A. 2018, MNRAS, 473, 1695
Dessart, L., & Hillier, D. J. 2020, A&A, 642, A33
Dessart, L., Hillier, D. J., Li, C., et al. 2012, MNRAS, 424, 2139
Dessart, L., Hillier, D. J., Livne, E., et al. 2011, MNRAS, 414, 2985
Dessart, L., Hillier, D. J., Sukhbold, T., et al. 2021, A&A, 656, A61
Dessart, L., Hillier, D. J., Waldman, R., et al. 2013, MNRAS, 433, 1745
Dessart, L., Hillier, D. J., Woosley, S., et al. 2015, MNRAS, 453, 2189
Dessart, L., Hillier, D. J., Woosley, S., et al. 2016, MNRAS, 458, 1618
Ennis, J. A., Rudnick, L., Reach, W. T., et al. 2006, ApJ, 652, 376
Ensman, L. M., & Woosley, S. E. 1988, ApJ, 333, 754
Fang, Q., & Maeda, K. 2018, ApJ, 864, 47
Fang, Q., Maeda, K., Kuncarayakti, H., et al. 2019, NatAs, 3, 434
Fang, Q., Maeda, K., Kuncarayakti, H., et al. 2022, ApJ, 928, 151
Filippenko, A. V. 1997, ARA&A, 35, 309
Fransson, C., & Chevalier, R. A. 1989, ApJ, 343, 323
Fremling, C., Sollerman, J., Taddia, F., et al. 2016, A&A, 593, A68
Galama, T. J., Vreeswijk, P. M., van Paradijs, J., et al. 1998, Natur, 395, 670
Gal-Yam, A. 2017, Handbook of Supernovae (Cham: Springer), 195
Groh, J. H., Georgy, C., & Ekström, S. 2013, A&A, 558, L1
Hamuy, M., Folatelli, G., Morrell, N. I., et al. 2006, PASP, 118, 2
Harris, C. R., Millman, K. J., van der Walt, S. J., et al. 2020, Natur, 585, 357
Heger, A., Fryer, C. L., Woosley, S. E., et al. 2003, ApJ, 591, 288
Hjorth, J., Sollerman, J., Møller, P., et al. 2003, Natur, 423, 847
Hunter, J. D. 2007, CSE, 9, 90
Jerkstrand, A. 2017, Handbook of Supernovae (Cham: Springer), 795
Jerkstrand, A., Ergon, M., Smartt, S. J., et al. 2015, A&A, 573, A12
Karamehmetoglu, E., Sollerman, J., Taddia, F., et al. 2022, arXiv:2210.09402
Kasen, D., & Woosley, S. E. 2009, ApJ, 703, 2205
Kifonidis, K., Plewa, T., Janka, H.-T., et al. 2003, A&A, 408, 621
Kifonidis, K., Plewa, T., Scheck, L., et al. 2006, A&A, 453, 661
Kilpatrick, C. D., Drout, M. R., Auchettl, K., et al. 2021, MNRAS, 504, 2073
Kuncarayakti, H., Maeda, K., Bersten, M. C., et al. 2015, A&A, 579, A95
Limongi, M., & Chieffi, A. 2003, ApJ, 592, 404
Lyman, J. D., Bersier, D., James, P. A., et al. 2016, MNRAS, 457, 328
Maeda, K., Kawabata, K., Tanaka, M., et al. 2007, ApJL, 658, L5
Maund, J. R., Fraser, M., Ergon, M., et al. 2011, ApJL, 739, L37
Maurer, J. I., Mazzali, P. A., Deng, J., et al. 2010, MNRAS, 402, 161
Mazzali, P. A., Deng, J., Maeda, K., et al. 2002, ApJL, 572, L61
Modjaz, M., Gutiérrez, C. P., & Arcavi, I. 2019, NatAs, 3, 717
Modjaz, M., Kewley, L., Kirshner, R. P., et al. 2008, AJ, 135, 1136
Moriya, T. J., Suzuki, A., Takiwaki, T., et al. 2020, MNRAS, 497, 1619
Morozova, V., Piro, A. L., Renzo, M., et al. 2015, ApJ, 814, 63
Nakamura, T., Mazzali, P. A., Nomoto, K., et al. 2001, ApJ, 550, 991
Paxton, B., Bildsten, L., Dotter, A., et al. 2011, ApJS, 192, 3
Paxton, B., Cantiello, M., Arras, P., et al. 2013, ApJS, 208, 4
Paxton, B., Marchant, P., Schwab, J., et al. 2015, ApJS, 220, 15
Paxton, B., Schwab, J., Bauer, E. B., et al. 2018, ApJS, 234, 34
Paxton, B., Smolec, R., Schwab, J., et al. 2019, ApJS, 243, 10
Piro, A. L., & Nakar, E. 2013, ApJ, 769, 67
Sana, H., de Mink, S. E., de Koter, A., et al. 2012, Sci, 337, 444
Sauer, D. N., Mazzali, P. A., Deng, J., et al. 2006, MNRAS, 369, 1939
Shigeyama, T., & Nomoto, K. 1990, ApJ, 360, 242
Shigeyama, T., Nomoto, K., Tsujimoto, T., et al. 1990, ApJL, 361, L23
Smartt, S. J. 2009, ARA&A, 47, 63
Smith, N. 2014, ARA&A, 52, 487
Sun, N.-C., Maund, J. R., & Crowther, P. A. 2023, MNRAS, 521, 2860
Taddia, F., Stritzinger, M. D., Bersten, M., et al. 2018, A&A, 609, A136
Taubenberger, S., Valenti, S., Benetti, S., et al. 2009, MNRAS, 397, 677
Teffs, J., Ertl, T., Mazzali, P., et al. 2020, MNRAS, 492, 4369
Valenti, S., Benetti, S., Cappellaro, E., et al. 2008, MNRAS, 383, 1485
Van Dyk, S. D., Zheng, W., Fox, O. D., et al. 2014, AJ, 147, 37
Virtanen, P., Gommers, R., Oliphant, T. E., et al. 2020, NatMe, 17, 261
Wongwathanarat, A., Müller, E., & Janka, H.-T. 2015, A&A, 577, A48
Woosley, S. E., & Bloom, J. S. 2006, ARA&A, 44, 507
Woosley, S. E., Heger, A., & Weaver, T. A. 2002, RvMP, 74, 1015
Woosley, S. E., & Weaver, T. A. 1995, ApJS, 101, 181
Yoon, S.-C. 2015, PASA, 32, e015
Yoon, S.-C., Chun, W., Tolstov, A., et al. 2019, ApJ, 872, 174